RSC Advances

PAPER

View Article Online
View Journal | View Issue

Cite this: *RSC Adv.*, 2026, **16**, 22310

Impedance spectroscopy investigations on the electrical response and morphology of $BiBaFeTiO_6$ double perovskite for multifunctional applications

Marwa Slimi * and Nizar Rammeh

$BiBaFeTiO_6$ was synthesized successfully through a sol–gel method. XRD examinations revealed that the compound exhibited a crystalline cubic double-perovskite structure with the space group $Pm\bar{3}m$. The morphology and elemental composition were examined using scanning electron microscopy (SEM), energy-dispersive X-ray spectroscopy (EDX), and elemental mapping. Results revealed that the material had a uniform distribution of elements and the predicted chemical composition. Electrical measurements were conducted in the temperature range of 373–453 K and the frequency range of 0.1 Hz to 1 MHz. The AC conductivity of $BiBaFeTiO_6$ was established using the correlated barrier hopping (CBH) model. Activation energies derived from DC conductivity and modulus spectra were comparable, indicating that both the relaxation process and electrical conduction originated from the same underlying mechanism. Furthermore, a thorough examination of the Nyquist plots showed the sensitivity of the material's electrical properties to changes in temperature and frequency. The sample's semiconducting nature was demonstrated by the resistivity and impedance NTCR (negative temperature coefficient of resistance) properties. The Nyquist plots ($-Z''$ *vs.* Z') display the contribution of grains and grain boundaries in the electrical conductivity, confirming the existence of a non-Debye-type relaxation. The non-overlapping small polaron tunneling (NSPT) process in $BiBaFeTiO_6$ is suggested by the value of the exponent "s", which denotes the conduction process described by the Correlated Barrier Hopping (CBH) model. This material's NTCR characteristics, including a good stability factor, thermistor constant, and sensitivity factor, may be beneficial for developing NTC-type thermistors.

Received 7th February 2026
Accepted 13th April 2026

DOI: 10.1039/d6ra01113f

rsc.li/rsc-advances

1. Introduction

Perovskites are among the most remarkable ferroelectric relaxor materials. Their diverse electrical properties—ranging from insulating and semiconducting to metallic and even superconducting—make them highly versatile and suitable for a wide range of applications, including solar cells, photodetectors, laser technologies, and X-ray imaging systems.[1] Perovskite materials typically adopt the ABO_3 formula. In contrast to the B-site occupants, which are commonly transition metals, the A site is generally occupied by one or more cations with a high ionic radius, such as alkaline earth metals.

Double perovskites are derived from the perovskite structure and exhibit the general formula of $AA'BB'O_6$, wherein distinct cations can alternately occupy the B sites. Large cations, such as Sr^{2+} and Ba^{2+}, reside at the A site, whereas less bulky cations, such as transition metals, occupy the alternating B and B′ sites, which are placed alternately in the structure. Due to their diverse applications and cost-effective synthesis, these materials have garnered significant interest. Additionally, they can accommodate additional cations at the A and/or B sites with minimal structural disruption. These perovskite oxide variants are under intensive investigation for diverse applications in next-generation electric devices owing to their exceptional chemical and physical properties.[2] Furthermore, they exhibit a range of distinct crystal structures, such as the rhombohedral systems like $BiBaNiMnO_6$,[3] $BiBa_{0.5}Ag_{0.5}Ni_2O_6$ (ref. 4) and $BiBaNiNbO_6$ (ref. 5) or cubic systems like $LaBa_{0.5}Ag_{0.5}FeMnO_6$ and Ba_2InNbO_6.[6,7] Single perovskites exhibit stability and chemical compatibility issues during their synthesis and operation. Consequently, double perovskites were developed to enhance perovskite performance.[8] This performance emanates from their composition and flexible structure, which facilitate diverse anionic and cationic substitutions. Hence, double perovskites are widely used in photocatalytic and photovoltaic applications due to their superior electrical conductivity and chemical stability.[9,10]

This compound has been of interest to many researchers thanks to its wide range of applications and low-cost synthesis. Moreover, it can accommodate different cations at A and/or B sites with minimal disruption to the structure. The material exhibits a wide spectrum of dielectric, ferroelectric, piezoelectric, pyroelectric, and electrostrictive properties arising from

Laboratory of Materials Physics (LPM), Faculty of Sciences, University of Sfax, B. P. 1171, 3000 Sfax, Tunisia. E-mail: msrammeh@yahoo.fr

structural distortions, including Jahn-Teller elongations, center-cation displacements, and oxygen-octahedral tilting.[11,12] Given the demand for multifunctional materials in practical applications, the incorporation of Ba^{2+} and Bi^{3+} at the A-site improves dielectric and ferroelectric ordering, while Fe^{3+} and Ti^{4+} at the B-site enhance the electrical and magnetic features in $BiTiO_3$ and $BiFeO_3$-based modulated perovskites.[13]

Impedance spectroscopy (IS) is a widely used method to analyze the electrical characteristics of a wide variety of double perovskite materials, whether ionic, semiconducting, or even insulating.[14] It provides information pertaining to the materials' volume composition as well as the electrical properties.

Therefore, the present study aims not only to develop a double-perovskite material $BiBaFeTiO_6$ (BBFTO) using the sol–gel technique but also to study its influence on this material's physical properties. Its ultimate objective is the analysis of its morphological and structural characteristics by X-ray diffraction and scanning electron microscopy. Furthermore, its complex electrical impedance spectrum enabled detailed analysis of its electrical and dielectric properties.

2. Experimental techniques

The precursors such as 0.073 M $Bi(NO_3)_3 \cdot 5H_2O$, 0.073 M $Ba(NO_3)_2$, 0.036 M Fe_2O_3 and 0.073 M TiO_2 of 99.9% purity were used in the sol–gel reaction to synthesize the samples of $BaBiFeTiO_6$. All reagents were of analytical grade (purchased from Sigma-Aldrich) and used as obtained without any further purification.[15]

$$Bi(NO_3)_3 + Ba(NO_3)_2 + 1/2Fe_2O_3 + TiO_2 \rightarrow BiBaFeTiO_6 + O_2 + NO_2$$

Following the determination of the precursors' proportions, they were weighed on a scale and then added to an Erlenmeyer flask fitted with a magnetic bar. 15 milliliters of distilled water and 30 milliliters of nitric acid were then added to this. A hot plate with a magnetic stirrer was used to dissolve this mixture at 75 °C for 4 h, and subsequently, ethylene glycol was added to accelerate gel formation. The resultant gel was gradually dried at 170 °C, and the ensuing mixture was heated to 500 °C for 6 h. The obtained powder was then crushed and pressed in a mold using 4 tons cm^{-2} to create round pellets after being baked for 12 hours twice at 1173 °C and 1223 °C, respectively (Fig. 1).

Although the same procedure and stages were used to prepare many samples, different chemical precursors were utilized. The prepared sample's structure, phase purity, and homogeneity were assessed by X-ray powder diffraction (XRD) examination using a Philips diffractometer. Additionally, a scanning electron microscope (SEM) was used for the morphological characterization to determine the particle sizes.

A broadband dielectric spectrometer (BDS) NoVo control Alpha analyzer was used to perform dielectric measurements at a frequency range of 10^{-1} to 10^6 Hz and temperatures ranging from 253 to 423 K. The present analysis was limited to the intermediate temperature range, where the material retains its structural integrity and reliable dielectric/electrical behavior. To this end, the $BiBaFeTiO_6$ sample was finely ground in a mortar to obtain a homogeneous powder, and then, this powder was pressed into pellets of approximately 1 mm thickness and 8 mm diameter under a pressure of approximately 3 T cm^{-2}. An alternate current was applied to a plate capacitor after sandwiching the sample between its parallel platinum electrodes. In a closed cryostat, a flow of pure nitrogen gas was used to regulate the temperature.

3. Analysis and experimental results

3.1. Structural and morphological analyses

3.1.1 X-ray diffraction of BBFTO. The XRD pattern of $BiBaFeTiO_6$ given in Fig. 2 reveals the absence of secondary phases, suggesting that the material is well-crystallized and single-phase. A good fit between the observed and the calculated profiles was obtained. The difference observed between the intensities of the measured and calculated diffraction lines can be attributed to the existence of preferential orientation of the crystallites in the sample.

The structure was refined using the Rietveld method with the FullProf software. This sample crystallized in a cubic structure with the space group of $Pm\bar{3}m$, according to XRD examination.[16] The extracted unit cell parameter of the examined pattern for

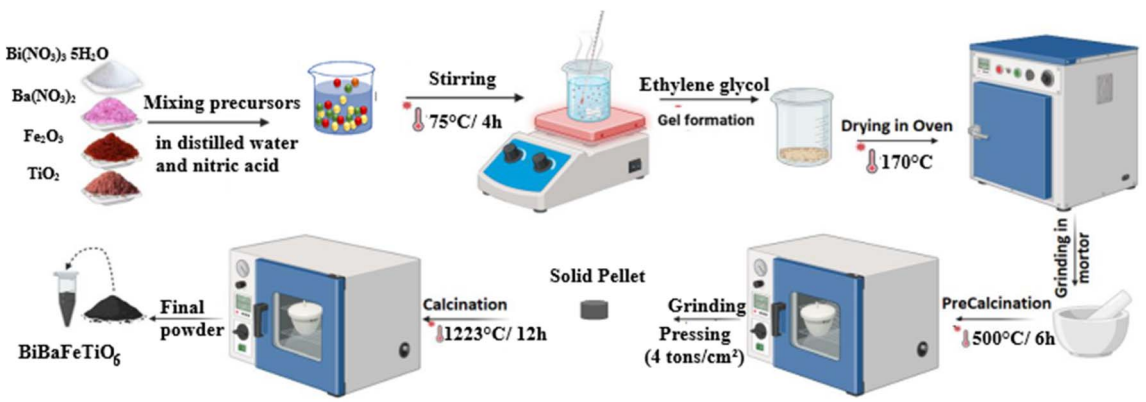

Fig. 1 Schematic of the sol–gel synthesis.

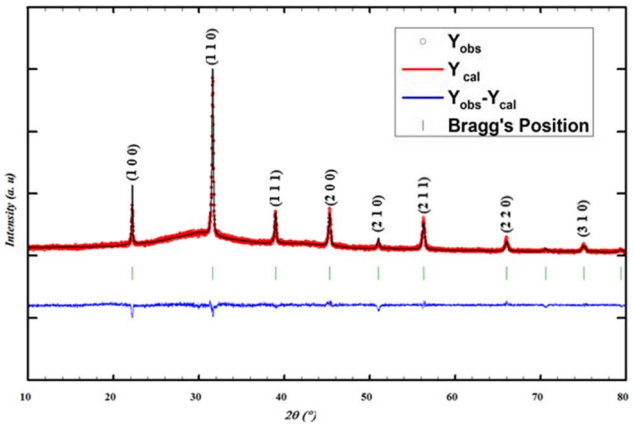

Fig. 2 Observed and calculated XRD profiles of $BiBaFeTiO_6$. Experimental points are shown by circles (○) and the calculated profile by a solid line. The bottom trace is the difference pattern, $y_{obs} - y_{cal}$, and the bars indicate the angular positions of Bragg reflections.

the sample BBFTO was $a = 3.9992$ Å with volume $V = 63.962$ A^3 and the reliability factor $\chi^2 = 1.86$.

In fact, the Goldschmidt tolerance factor t was computed[17] and provided by the following formula to verify the presence of the perovskite-like structure and the extent of distortion in this compound:

$$t = \frac{r_A + r_O}{\sqrt{2}(r_B + r_O)} \quad (1)$$

As defined by Shannon, ionic radii are: $r\langle Bi^{3+}\rangle = 1.36$ Å, $r\langle Ba^{2+}\rangle = 1.61$ Å, which represents r_A, $r\langle Fe^{3+}\rangle = 0.64$ Å, $r\langle Ti^{4+}\rangle = 0.6$ Å, which stands for r_B and $r\langle O^{2-}\rangle = 1.4$ Å.[18] The cubic structure of this material is confirmed by a t value greater than 1.

The double perovskite $BiBaFeTiO_3$ shows significant differences from single perovskites like $BiFeO_3$ or $BaTiO_3$. It crystallizes in the ABO_3 structure with a single B-site cation.[11,12] These changes stem from the presence of two distinct cations (Fe^{3+} and Ti^{4+}) occupying the B-site positions. The XRD pattern shows minor shifts in peak locations (2θ) and changes in peak intensities due to the structural distortions caused by this cationic ordering or partial disorder. Furthermore, compared to the more straightforward $BiTiO_3$ structure, the addition of Ba^{2+} at the A-site and the mixed B-site occupancy cause a lattice deformation (Table 1). These distortions can reduce the symmetry from the ideal cubic perovskite structure to pseudo-cubic or orthorhombic, often altering the lattice properties. Peak broadening or asymmetry in specific diffraction peaks exemplifies these effects. The observed improvements in its electrical and dielectric behaviour, which underpin its potential for multifunctional applications, arise from these structural changes.

3.1.2 SEM and EDX analyses. The size and shape of the BBFTO nanoparticles were examined using scanning electron microscopy (SEM). The sample microstructure's homogenous granular distribution is depicted in Fig. 3a. Additionally, elemental colour mapping was employed to further examine elemental distributions. Fig. 3a shows the apparent uniform distribution of desirable components across the compound's surface, which demonstrates that all the constituent elements of the sample, including Bi, Ba, Ti, Fe, and O, were uniformly distributed. The particle size distribution is statistically represented by the histogram in Fig. 3b. It is fitted using a Lorentzian function and generated with ImageJ software, which allows us to determine the average particle size D_SEM $\sim$ 0.41 μm. Energy-dispersive X-ray spectroscopy (EDS) enabled us to precisely evaluate the elemental composition of the synthesized sample, as illustrated in Fig. 3c. The occurrence of X-ray peaks corresponding to different atoms confirms the compound's purity and demonstrates its homogeneous, proportional distribution across grains and grain boundaries.[19]

3.2. Impedance spectrum analysis

Impedance spectroscopy is a crucial technique for researching a material's electrical characteristics. It enables us to detect changes in a number of characteristics, including capacitance and resistance, at varying frequencies and with a low amplitude stimulation.[20] The real component of impedance (Z') as a function of frequency at different temperatures is shown in Fig. 4a. In these variations in impedance Z' of our sample, two distinct zones are shown. Because of the strong charge-carrier mobility, which suggests an increase in AC conductivity with temperature and frequency, the first zone (I) is at low frequency, where the values of Z' steadily decrease with the increase in frequency and temperature.[21–23] The Z' fuses at higher frequencies (II) irrespective of temperature. As the material's barrier qualities deteriorate at higher temperatures, space charge may be released, which can be attributed to space charge polarization.[24,25]

Measurements of the imaginary impedance (Z'') of the $BiBaFeTiO_6$ sample are given in Fig. 4b, providing useful insights into the temperature-dependent electrical behavior of

Table 1 Structural properties and synthesis methods of the compounds $BiBaFeTiO_6$, $BiFeO_3$ and $BaTiO_3$

	Crystal structure	Lattice parameter (Å)	Space group	Synthesis method	References
$BiBaFeTiO_6$	Cubic	3.9992	$Pm\bar{3}m$	Sol–gel	Our work
$BiFeO_3$	Rhombohedral	$a \approx 5.58$ $c \approx 13.90$	$R3c$	Sol–gel	12
$BaTiO_3$	Tetragonal	$a \approx 3.99$ $c \approx 4.03$	$P4mm$	Sol–gel	11

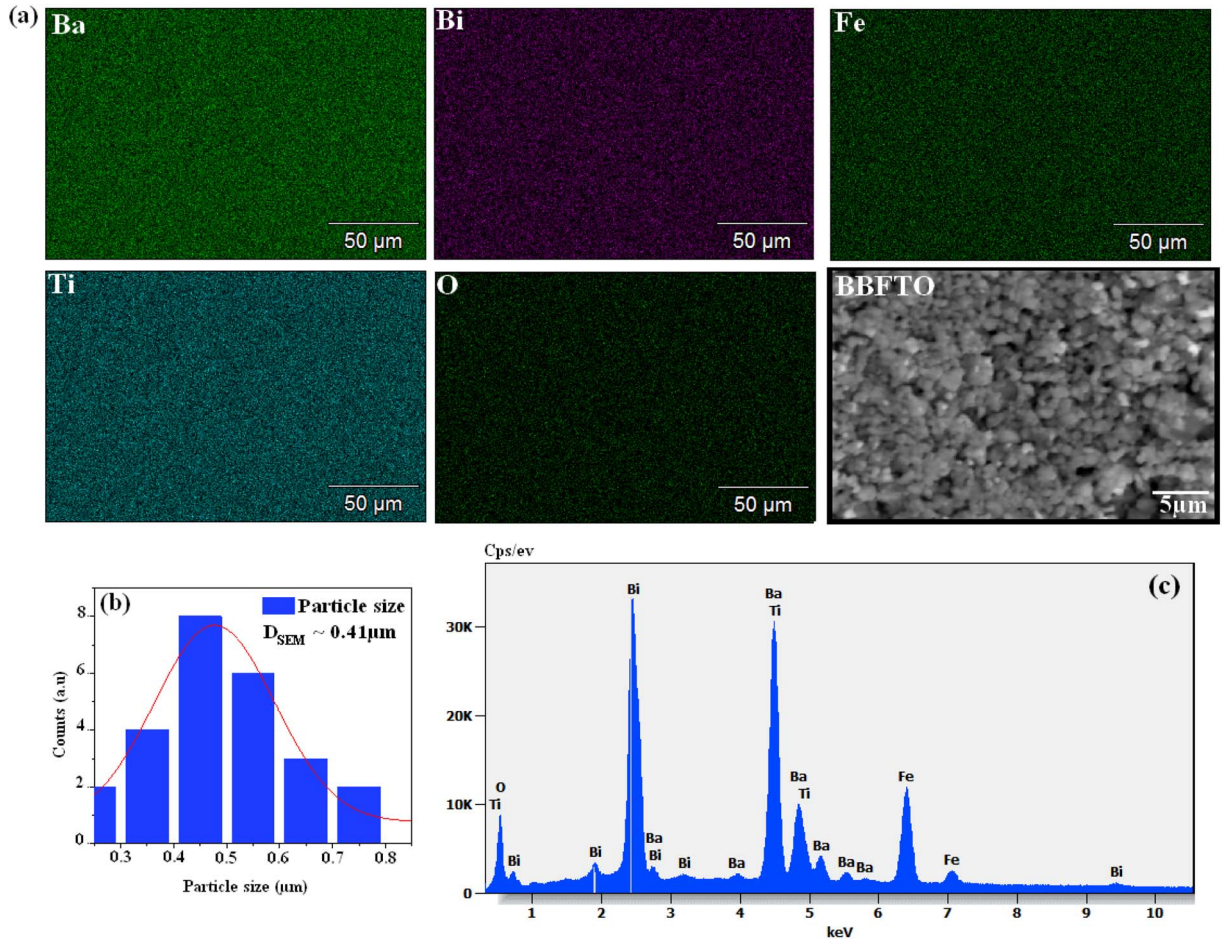

Fig. 3 : (a) EDS map of $BiBaFeTiO_6$. (b) Histogram of the grain-size distribution. (c) EDS spectrum of $BiBaFeTiO_6$ prepared by the sol–gel method.

the produced material. When the Z'' spectrum is plotted against frequency, clear patterns emerge, which provide insight into the BBFTO sample's electrical properties. Significantly, at lower temperatures, the Z'' spectrum shows noticeable peaks. It is evident that these peaks change and become more flattened as the temperature increases. This finding implies that when the temperatures rise, the peaks become wider. Practically speaking, this means that the material's electrical response changes with the increase in temperature, resulting in a more evenly distributed dispersion of energy across a variety of frequencies. This variation indicates a temperature-dependent electrical relaxation process within the material. The asymmetric broadening of the peak with increasing temperature reflects a temperature-dependent distribution of relaxation times. In simpler terms, the observed shifts and broadening of peaks in the Z'' spectrum result from temperature-induced

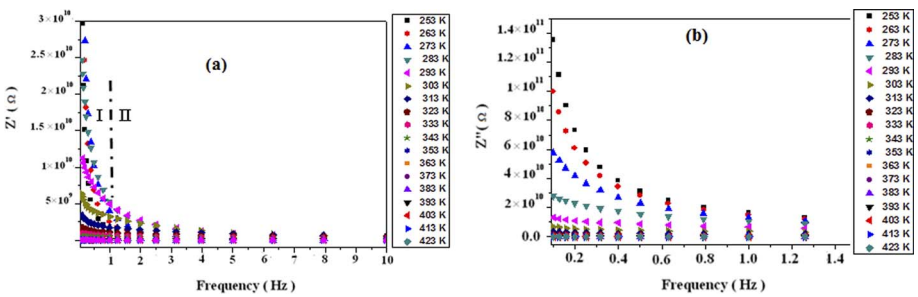

Fig. 4 (a) Variation in the real part of impedance as a function of frequency at various temperatures. (b) Variation in the imaginary part ($-Z''$) of impedance as a function of frequency at various temperatures.

changes in the material's electrical conductivity.[26–28] Temperature-dependent electrical relaxation is essential for understanding the material's dynamic response to varying thermal conditions.[29,30] The intricate relationship between temperature and the sample's electrical characteristics is highlighted by the observed variations in the Z'' spectrum.

There may be one or more semicircles in the ceramics' impedance charts. Notably, compared to grain interiors, the grain boundaries in ceramics have a larger density of structural and chemical flaws, making them more resistant. As a result, at high frequencies, while grain boundaries are accredited to a greater dimension semicircle, grain interiors are attributed to a smaller diameter semicircle.[31] As shown in Fig. 5a and b, the Nyquist plot illustrates the relationship between Z' and Z'' at various temperatures (253–423 K) spanning the frequency range of 10^{-1} Hz–10^{6} Hz. The semicircle arcs in the impedance spectra, which correspond to the grain boundary contribution, are clearly visible in this illustration.

The subtle variations in the Nyquist plot as a function of temperature enable a comprehensive understanding of the material's dynamic electrical response under diverse thermal conditions. The Nyquist diagram reveals the existence of two separate semicircles in Fig. 5a. The first semicircle, observed at higher frequencies, indicates the influence of grain boundaries on the conduction process and depends on grain presence. The electrode effect is responsible for the second semicircle, which is visible at lower frequencies.[32] These curves' experimental points are derived from the circular arcs whose centers lie below the real axis and which pass close to the origin. The Debye plots' production of semicircles with the real axis at their center indicates that the material behaves in accordance with the Cole–Cole model. As the temperature rises, resistance decreases, signifying the thermal activation of the material's conductivity. Using the *Z*-view program, an equivalent circuit (Fig. 5b) was created to illustrate the material's electrical behavior. To obtain the proper fit, we used an analogous circuit, which is a combination series of two circuits—one grain (R1–C1) and two grain boundaries (R2–CPE1/R3–CPE2), where R is the resistance and CPE is the constant phase element that corresponds to the complex element.[33]

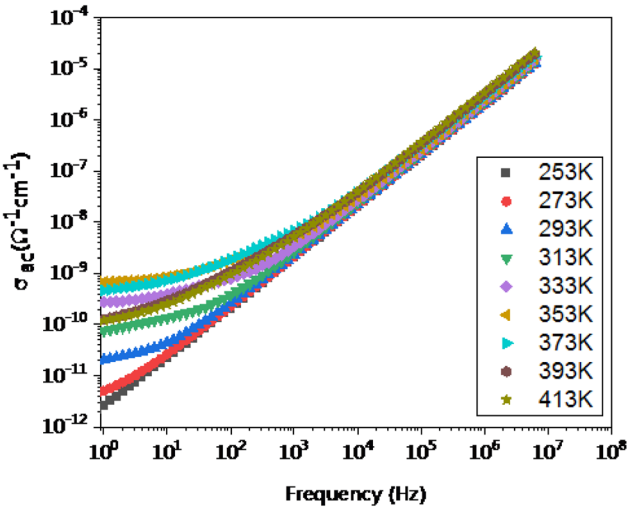

Fig. 6 Variation in the AC conductivity (σ_{AC}) of $BiBaFeTiO_6$ with frequency at selected temperatures.

3.3. Conductivity studies

An important source of information on the charge-transport mechanism and the interactions between charge carriers within a material is the analysis of conductivity variations as a function of alternating current (AC) frequency. The orderly mobility of weakly bonded charged particles under the influence of an electric field is typically the cause of electrical conduction in dielectrics. Our sample, $BiBaFeTiO_6$, contains a variety of chemical linkages, primarily covalent and ionic. This variation is likely to emanate from the weakest ionic bond in the sample—the one between the bulkiest Ba^{2+} cation and oxygen. To further understand how these interactions affect the conduction process, it is crucial to examine electrical conductivity as a function of temperature and frequency. The displayed conductivity spectra offer sophisticated insights into the material's electrical activity.

Two separate contributions may be seen in the conductivity spectra displayed in Fig. 6: a highly dispersive component, known as the AC conductivity, and a frequency-independent component (at low frequencies), known as the DC conductivity. Due to the increased mobility of the charge carriers, we can observe an increase in the conductivity as a function of

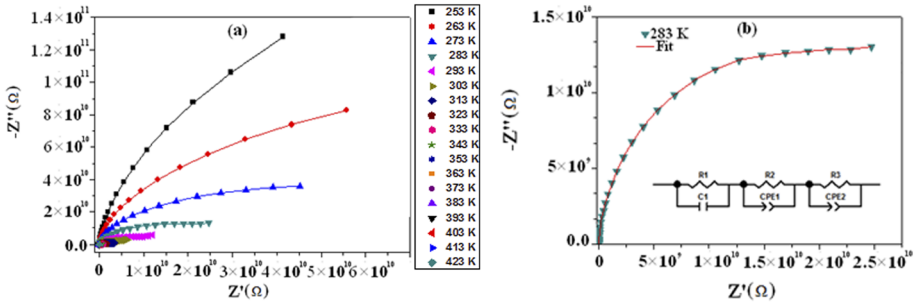

Fig. 5 (a) Complex impedance plot of $BiBaFeTiO_6$ at different temperatures. (b) Impedance diagram at 283 K.

temperature from 2.55 × 10^{-12} Ω^{-1} cm^{-1} at 253 K to 6.75 × 10^{-10} Ω^{-1} cm^{-1} at 413 K, as the annealing temperature rises. The increase in electrical conductivity with temperature observed in $BiBaFeTiO_6$ can be attributed to the thermally activated transport, which is a typical mechanism of semiconducting oxide materials. As the temperature increases, more charge carriers gain sufficient thermal energy to overcome the potential barriers between localized states, which enhances both the carrier mobility and the hopping probability between ions (such as Fe^{3+}/Fe^{2+} or Ti-related sites). The conductivity has a steady and homogeneous profile in the high-frequency band, increasing gradually, irrespective of temperature, to a maximum of 2.079 × 10^{-5} Ω^{-1} cm^{-1}. Moreover, the conductivity curves can be expressed using the Jonscher relation:[34,35]

$$\sigma_{AC} = \sigma_{DC} + A\omega^{S} \quad (2)$$

where A is a temperature-dependent constant, ω is the frequency, σ_{DC} is the DC conductivity, and s ($0 \leq s < 1$) is a dimensionless parameter that describes the dispersion in the material.

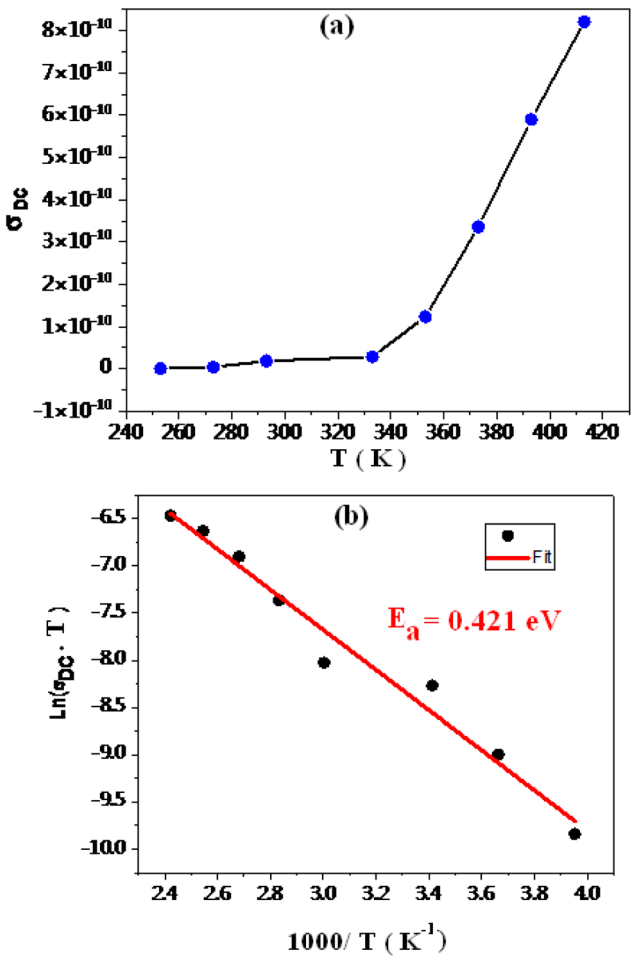

Fig. 7 (a) Variation in the DC conductivity (σ_{DC}) at different temperatures. (b) Temperature dependence of ln ($\sigma_{DC} \times T$).

According to the Arrhenius law, the temperature dependence of dc conductivity, shown in Fig. 7a, exhibits an exponential relationship with temperature. The Arrhenius equation can be used to characterize this variation as follows:[36–38]

$$\sigma_{DC} \times T = \sigma_0 \, e^{-\frac{E_a}{k_B T}} \quad (3)$$

where E_a is the activation energy, k_B is the Boltzmann constant, and σ_0 is the pre-exponential factor.

The semi-logarithmic curve of ($\sigma_{dc} \times T$) as a function of 1000/T was plotted in order to determine the activation energy E_a, as seen in Fig. 7b. By calculating the slope of the linear fit from the traced curve, E_a was found to be 0.421 eV. This large activation energy suggests a significant energy barrier for charge carriers, which has significant ramifications, especially in thermoelectric applications.[39,40] High activation-energy materials are attractive for thermoelectric device applications because they prevent heat diffusion and encourage effective electrical conduction, making their understanding and use essential to improving thermoelectric efficiency.

An outstanding source of information regarding the model for the conduction process in the material is the exponent "s", which stands for the degree of interaction between ions and their surroundings. As shown in Fig. 8, two different behaviors can be identified for this sample. The correlated barrier hopping (CBH) model may adequately reflect the conduction process in this range, as evidenced by the fact that "s" clearly decreases with the decrease in temperature T below 350 K.[41] Non-overlapping Small Polaron Tunneling (NSPT),[42] which is pertinent for researching conduction phenomena in the boundary of the alternating regime, appears to be the optimal conduction model, as the situation deteriorates with rising temperature for T > 350 K.

3.4. Dielectric studies

Fig. 9a illustrates how the real part of the dielectric permittivity ε' changes with frequency at various temperatures. The dielectric polarization process of the material can account for the observation that ε' declines exponentially with the increase in

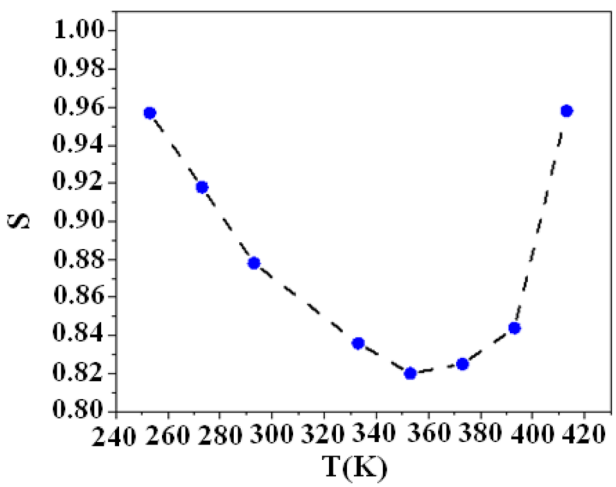

Fig. 8 Temperature dependence of the exponent S for $BiBaFeTiO_6$.

frequency and approaches a constant value at higher frequencies. This is probably explained by the material's dielectric polarization process. At low frequencies, the values of ε' are actually very high due to the buildup of charge carriers between the electrodes and sample.[43]

The complex permittivity's imaginary part ε'' varies with frequency at various temperatures, as seen in Fig. 9b. In fact, there is a discernible reduction in ε'' with the increase in frequency, peaking at $T = 363$ K. Both the relaxation time distribution and charge carrier density are responsible for this.[44] Furthermore, this variation can be explained by the electron exchange between Fe^{2+} and Fe^{3+} species, which increases the dipoles' orientation and causes charges to accumulate at the grain-to-grain interface and grain boundaries, giving rise to various forms of polarization, including electronic, ionic, and interfacial (electrode) polarization.[45] However, because the exchange between the Fe^{2+} and Fe^{3+} species does not follow the alternating applied electric field in the high-frequency zone, the dielectric constant remains constant over the studied temperature range.[46,47]

3.5. Electrical modulus studies

The experimental results can also be analyzed using the complex modulus formalism. This approach circumvents issues such as electrode polarization and offers a different perspective on electrical properties.[48,49] Eqn 4 was used to calculate the real and imaginary components of the modulus $M^*(\omega)$ from the permittivity $\varepsilon^*(\omega)$:

$$M^* = M' - jM'' \frac{1}{\varepsilon^*} \quad (4)$$

$$M' = \frac{\varepsilon'}{\varepsilon'^2 + \varepsilon''^2} \quad (5)$$

$$M'' = \frac{\varepsilon''}{\varepsilon'^2 + \varepsilon''^2} \quad (6)$$

where M' and M'' stand for the real and imaginary components of the electric modulus, respectively.

The influence of the real component (M') of the modulus as a function of frequency throughout a temperature range of 253–423 K is depicted in Fig. 10a. Due to the slower relaxation processes, such as ion migration or dipolar reorientation, at low frequencies, M' tends to approach zero, which indicates that electrode polarization and long-range charge-carrier migration dominate the electrical response. As the frequency increases, M' gradually rises owing to the diminished contribution of electrode polarization and the increasing dominance of bulk relaxation processes. The temperature dependence further confirms that the relaxation mechanism is thermally activated,

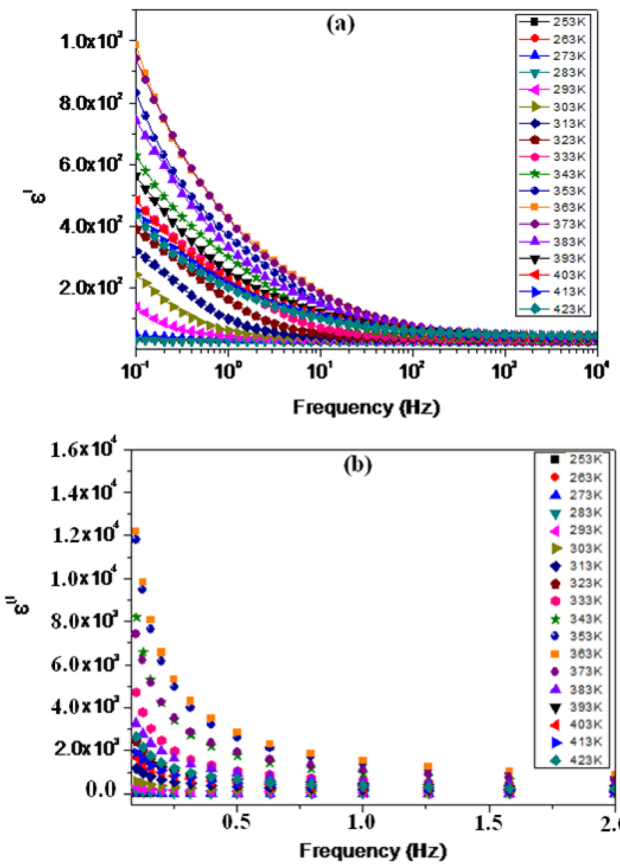

Fig. 9 (a) Dielectric constant's frequency-dependent real part (ε') and (b) imaginary part (ε'') at various temperatures for BBFTO.

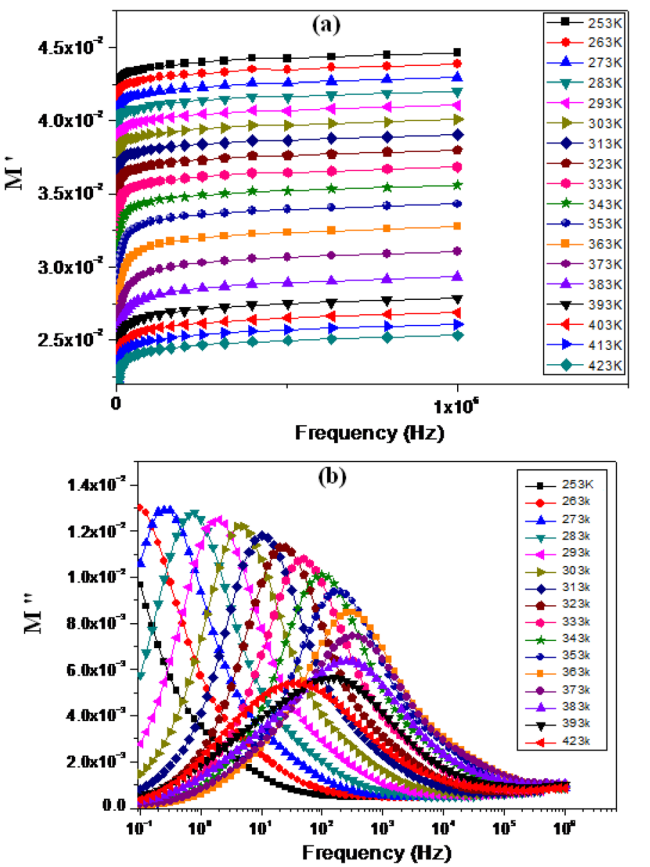

Fig. 10 (a) Real part of the electrical modulus (M') and (b) imaginary part of the modulus (M'') as a function of frequency at different temperatures.

where increasing temperature enhances the mobility of the charge carriers and facilitates their hopping between localized sites.

The dependence of the imaginary part of the modulus M'' on frequency (Fig. 10b) reveals a relaxation process.[50] M'' has an asymmetric peak at a certain temperature. At different temperatures, M'' increases with frequency up to a maximum peak, M_{max}'', and then decreases. On the other hand, the position of the relaxation peak shifts to higher frequencies as the temperature increases up to $T = 363$ K. Above this temperature, the peak maximum shifts toward lower frequencies, indicative of a temperature-dependent relaxation process. The frequency region below the M'' peak corresponds to the range where polarons drift over long distances, whereas the region above the peak reflects polaron confinement within potential wells, allowing localized motion.

4. Conclusion

In the present research work, $BiBaFeTiO_6$ with a pure double-perovskite phase was successfully synthesized at 1300 °C using a sol–gel method. The material's pure cubic $Pm\bar{3}m$ phase was validated by structural refinement analyses and X-ray diffraction (XRD). Additionally, the uniform chemical composition and purity of the preparation were confirmed by the EDX results. The BBFTO compound's dielectric behavior and AC conductivity were investigated in relation to temperature and frequency in the ranges of 253 K–423 K and 10^{-1} Hz–10^6 Hz, respectively. Additionally, complex impedance analysis allows us to identify an equivalent electrical circuit specific to $BiBaFeTiO_6$ electrochemical cell. This circuit was composed of two circuits: a combination of R1–C1 and two grain boundaries (R2–CPE1/R3–CPE2). The fluctuation in the inferred $s(T)$ values indicated that the CBH model best describes the charge-transport mechanism in the prepared sample. However, when $T > 350$ K, the best conduction model was the non-overlapping small polaron tunneling (NSPT). To confirm that the relaxation mechanism involves the same type of charge carriers, the activation energy was determined using the alternating current conduction σ_{dc}.

Conflicts of interest

There are no conflicts to declare.

Data availability

The data that support the findings of this study are available from the corresponding author, Marwa SLIMI, upon reasonable request.

References

1 N. S. Kumar and K. C. B. Naidu, *J. Materiomics*, 2021, **7**, 940–956.
2 A. El Rharib, A. Amine, A. Oukerroum, M. A. Kinani, Y. Mir and M. Zazoui, *J. Comput. Condens. Matter*, 2022, **33**, 744.
3 K. Iben Nassar, M. Slimi, N. Rammeh, S. Soreto Teixeira and M. P. F. Grac, *Mater. Sci.:Mater. Electron.*, 2022, **33**, 1–11.
4 K. M. Krishna, K. Kumar, S. M. H. Qaid, N. N. Asemi, Y. Veeraswami, V. Kumar Arepalli and A. Kumar, *Opt. Mater.*, 2024, **154**, 115623.
5 J. P. Nayak, P. Agnihotri, S. Kumari, P. Kumari, P. Kumar and R. Rai, *J. Ceram. Int.*, 2024, **50**, 52682–52694.
6 K. Iben Nassar, N. Rammeh, S. Soreto Teixeira and M. P. F. Grac, *J. Electron. Mater.*, 2022, **51**, 370–377.
7 A. Dixit, J. A. Abraham, M. Manzoor, M. Altaf, Y. A. Kumar and R. Sharma, *J. Mater. Sci. Eng. B*, 2024, **307**, 117530.
8 L. Durai and S. Badhulika, *Sens. Actuators, B*, 2020, **325**, 128792.
9 S. S. Nair, L. Krishnia, A. Trukhanov, P. Thakur and A. Thakur, *J. Ceram. Int.*, 2022, **48**, 34128–34147.
10 M. Saniya, I. Sadiq, S. Shaheen, S. Khatoon and T. Ahmad, *Mater. Today Catal.*, 2024, **7**, 100067.
11 T. Hoshina, S. Hatta, H. Takeda and T. Tsurumi, *Jpn. J. Appl. Phys.*, 2018, **57**, 9.
12 V. Purohit and R. N. P. Choudhary, *Mater. Chem. Phys.*, 2020, **256**, 123732.
13 Z.-X. Chen, Y. Chen and Y. S. Jiang, *J. Phys. Chem. B*, 2002, **106**(39), 9986–9992.
14 M. Mohamed, K. Iben Nassar, M. Mohamed, N. Rammeh and M. P. F. Graça, *J. Mol. Struct.*, 2022, **1258**, 132658.
15 A. K. Yedluri and H.-J. Kim, *Dalton Trans.*, 2018, **47**, 15545–15554.
16 Z. ul Islam and B. Want, *J. Ceram. Int.*, 2025, **51**, 1585–1594.
17 V. M. Goldschmidt, *Geochemische Verteilungsgesetetze der Element VII, VIII*, Akad, Oslo, 1926.
18 M. D. Ingram, *J. Phys. Chem. Glasses*, 1987, **28**, 215.
19 M. Ben Abdessalem, S. Chkoundali, A. Oueslati and A. Aydi, *RSC Adv.*, 2022, **12**, 27154.
20 C. K. Lenka and S. K. Parida, *RSC Adv.*, 2026, **16**, 5535–5547.
21 B. K. Das, T. Das, K. Parashar, S. K. S. Parashar, R. Kumar, H. K. Choudhary, V. B. Khopkar, A. V. Anupama and B. Sahoo, *Mater. Chem. Phys.*, 2019, **221**, 419.
22 A. Hooda and M. S. Rathore, *Appl. Phys. A*, 2024, **130**, 666.
23 P. Mishra, D. Panda, S. S. Hota, L. Biswal, S. Joshi, A. Shukla and R. Naresh Prasad Choudhary, *J. Mater. Sci.:Mater. Electron.*, 2024, **35**, 2174.
24 M. Mahapatra, D. K. Pati, B. Sahu, P. Kumar Sahoo, R. K. Parida, B. N. Parida and R. Padhee, *J. Mater. Sci.: Mater. Electron.*, 2024, **35**, 582.
25 K. Iiker, *Microsc. Res. Tech.*, 2021, **84**, 3078–3086.
26 M. Slimi, M. M. Bouzayani, A. Oueslati and N. Rammeh, *J. Ceram. Int.*, 2026, **52**, 4800–4807.
27 S. Wang, J. Zhang, O. Gharbi, V. Vivier, M. Gao and M. E. Orazem, *Nat. Rev. Methods Primers*, 2021, **1**, 41.
28 D. Triyono, H. Laysandra, H. L. Liu and A. W. Anugrah, *J. Mater. Sci.: Mater. Electron.*, 2019, **30**, 18584–18598.
29 M. Younes, M. Nadeem, M. Atif and R. Grossinger, *J. Appl. Phys.*, 2010, **109**, 93704.
30 M. Nadeem and M. J. Akhtar, *J. Appl. Phys.*, 2008, **104**, 103713.
31 G. Catalan and J. F. Scott, *J. Adv. Mater.*, 2009, **21**, 2463–2485.

32 S. Feliu, J. Galván and M. Morcillo, *J. Corros. Sci.*, 1990, **30**, 989–998.
33 C.-H. Yang, D. Kan, I. Takeuchi, V. Nagarajan and J. Seidel, *J. Phys. Chem.*, 2012, **14**, 15953–15962.
34 A. K. Jonscher, *Dielectric Relaxation in Solids*, Chelesa Dielectric Press, London, 1983.
35 S. Sahoo, S. Mishra, H. Chouhan, N. C. Nayak, B. N. Parida, R. Padhee, S. K. Parida and R. Parida, *RSC Adv.*, 2025, **15**, 27467–27485.
36 G. Singh, V. S. Tiwari and P. K. Gupta, *J. Appl. Phys.*, 2010, **107**, 064103.
37 R. Kumari, N. Ahlawat, A. Agarwal, S. Sanghi and M. Sindhu, *J. Alloys Compd.*, 2017, **695**, 3282–3289.
38 B. C. Sutar, R. N. P. Choudhary and P. R. Das, *J. Ceram. Int.*, 2014, **40**, 7791–7798.
39 J. Wei, Q. Zhang, L. Zhao, L. Hao and C. Yang, *J. Ceram. Int.*, 2016, **42**, 11568–11573.
40 N. Mitoma, S. Aikawa, W. Ou-Yang, X. Gao, T. Kizu, M. F. Lin, A. Fujiwara, T. Nabatame and K. Tsukagoshi, *J. Appl. Phys. Lett.*, 2015, **106**, 042106.
41 S. Steinsvik, R. Bugge, J. Gjonnes, J. Tafto and T. Norby, *J. Phys. Chem. Solids*, 1997, **58**, 969–976.
42 A. Ghosh, *Phys. Rev. B:Condens. Matter Mater. Phys.*, 1990, **41**, 1479.
43 M. P. F. Graca, P. R. Prezas, M. M. Costa and M. A. Valente, *J. Sol-Gel Sci. Technol.*, 2012, **64**, 78.
44 X. Qian, N. Gu, Z. Cheng, X. Yang, E. Wang and S. Dong, *Electrochim. Acta*, 2001, **46**, 1829.
45 N. K. Singh, P. Kumar and R. Rai, *J. Alloys Compd.*, 2011, **509**, 2957.
46 M. Idrees, M. Nadeem, M. Atif, M. Siddique, M. Mehmood and M. M. Hassan, *Acta Mater.*, 2011, **59**, 1338.
47 J. Chemek, S. M. Borchani and M. Megdiche, *J. Electroceram.*, 2019, **42**, 165–177.
48 M. Ganguli, M. H. Bhat and K. J. Raol, *J. Phys. Chem. Glasses*, 1999, **40**, 297–304.
49 Y. Longhai and L. Qi, *AIP Adv.*, 2021, **11**, 125313.
50 M. Arora, V. Arora, S. Kaur, J. Kaur, S. Kumar and A. Singh, *Mater. Today: Proc.*, 2023, **80**, 1079–1085.